Unraveling Magnetic Anomalies: A Study of Earth's Field Asymmetries during the Laschamps Excursion

Alexander Rydh

**Dissertations in Geology at Lund University,
Bachelor's thesis, no 686
(15 hp/ECTS credits)**

Unraveling Magnetic Anomalies: A Study of Earth´s Field Asymmetries during the Laschamps Excursion

Bachelor's thesis
Alexander Rydh

Department of Geology
Lund University
2024

Contents

Cover Picture: Borealis from Jürg beer et al., (2011).

Abstract

Alexander Rydh

Abstract: Extreme geomagnetic variations such as excursions where the magnetic poles shift, and return are not fully understood. ^{10}Be, used as a proxy for the magnetic field studies has been proposed as a compliment to paleomagnetic models, allowing adjustments. LSMOD.2 is a sediment and volcanic based magnetic model encompassing the Laschamps excursion ~41 000 years ago. LSMOD.2 is limited due to lacking data from the high latitudes and the southern hemisphere, creating uncertainties in the model. To investigate the usefulness of ^{10}Be data, corrections must be made for climate variability, affecting the transport and deposition of ^{10}Be, as well as filtering for solar activity, occurring as millennial and centennial variations. In this study, ^{10}Be flux data shows good agreement with LSMOD.2 between 40.5 to 41.2 ka. After 41.2 ka the Greenland and Antarctica data diverge in ^{10}Be production rates with LSMOD.2. Comparing ^{10}Be data with other magnetic field reconstructions shows that LSMOD.2 has the best agreement over a period ca. 700 years. However, while LSMOD.2 does show the best agreement with ^{10}Be data, none of the investigated magnetic field models show an overall good agreement with ^{10}Be data or each other, thus ^{10}Be data is limited to uses for local models e.g. northern hemisphere.

Alexander Rydh, Department of Geology, Lund University, Sölvegatan 12, SE-223 62 Lund, Sweden. E-mail: al1745ry-s@student.lu.se

Sammanfattning

Alexander Rydh

Sammanfattning: Extrema geomagnetiska variationer som exkursioner där magnetfältet påbörjar en polomkastning, vilken avbryts är fortfarande oförstådda. ^{10}Be, som används som en proxy för magnetfälts studier har föreslagits som ett komplement till existerande paleomagnetiska modeller, vilket tillåter förbättring av modeller. LSMOD.2 är en sådan paleomagnetisk modell som baseras på sediment och vulkaniska data över Laschamps exkursionen för ~41 000 år sedan. LSMOD.2 saknar data från höga latituder och från södra hemisfären, vilket skapar osäkerheter i modellerna. För att undersöka om ^{10}Be från Antarktis och Grönland kan användas för att förbättra modellerna måste ^{10}Be data först korrigeras för klimatvariabler som påverkar transporten och depositionen av ^{10}Be och filtreras för att ta bort variationer som är orsakade av förändringar i solaktivitet som fluktuerar på relativt sett kortare (<500år) tidsskalor. I denna studie visar ^{10}Be flux data liknande värden som LSMOD.2 mellan 40 500 och 41 200 år sedan. Efter denna period divergerar ^{10}Be data från Grönland och Antarktis från LSMOD.2. Vid jämförelse med andra magnetfältsmodeller uppvisar LSMOD.2 längst överenstämmelse på 700 år med ^{10}Be data. Även då LSMOD.2 visar bäst överenstämmelse, uppvisas fortfarande brister i ^{10}Be data, då överlag ingen av magnetfältsmodellerna stämmer överens med ^{10}Be data eller varandra. På grund av detta är ^{10}Be data begränsat till lokala modeller som över norra hemisfären.

Alexander Rydh, Geologiska institutionen, Lunds universitet, Sölvegatan 12, 223 62 Lund, Sverige. E-post: al1745ry-s@student.lu.se

1 Introduction

Since the 1930s, it has been known that cosmic radiation from space is deflected by the Suns and Earth's magnetic fields. Despite the magnetic field acting as a shield, some of the cosmic radiation can still penetrate into Earth's atmosphere, initiating interactions with particles there. A consequence of this is the creation of cosmogenic radionuclides (Beer et al., 2011). Cosmogenic radionuclides are of keen interest in Earth sciences due to their isotopic and radioactive nature, acting as tracers for example the paleomagnetic field. As a result, these radiogenic isotopes have been thoroughly studied and we now have a firm grasp on their radioactive-deca$y$ (e.g. ^{10}Be with a half-life of $T_{1/2}$=1390000 years) and their production rates over the past millennia (Muscheler, 2013). Cosmogenic radionuclides such as ^{10}Be, ^{14}C and ^{36}Cl are preserved in various geological archives such as in ice cores and tree rings. Due to this fact, scientists have been able to measure their quantity, thus indirectly measuring Earth's magnetic fields variations through long time spans, compared to sunspot studies limited to ~400 years (Beer et al., 2011).

Studies on Earth´s paleomagnetic field have revealed that the geomagnetic field is not static, undergoing both long-term and short-term changes. Extreme variations such as excursions and reversals, where Earth´s magnetic poles swap places, are still not fully understood. Combined with paleomagnetic studies of rocks, scientists are researching how and why such variations arise, through modelling of the magnetic field. Despite this, problems arise due to a lack of paleomagnetic data in the southern hemisphere (Korte et al., 2019) As a result of this, records of ^{10}Be deposited in polar ice cores have been proposed as a compliment, being an independent signal which, at least hemispherically reflect the changes in the Earth's magnetic field (Nilsson et al., 2024).

In order for ^{10}Be records to be used a compliment to paleomagnetic reconstructions of Earth's magnetic field, requires correction taking into account its geochemical behaviour. This is a consequence of cosmogenic radionuclides transport and deposition being affected by the climate, creating hemispherical differences in ^{10}Be deposition on Antarctica and Greenland (Masarik & Beer, 1999).

In this study ^{10}Be data from Raisbeck et al. (2017) and Muscheler et al., (2004) will be compared to a pre-existing paleomagnetic field model called LSMOD.2 (based on volcanic and sediment data) during an excursion, in this case the Laschamps excursion ~41 ka (Panovska et al., 2023). By investigating asymmetries predicted by LSMOD.2 and implied by comparing ^{10}Be data from Greenland and Antarctica, the findings could prove the possible use of ^{10}Be data as a compliment to paleomagnetic models. This is a result of ~95% of ^{10}Be deposition in the polar ice caps coming from the same hemisphere, reflecting hemispherical production rates instead of global (Nilsson et al., 2024).

If ^{10}Be data represent variations in production rate as opposed to being affected by climate variability, it could be used as an independent signal together with LSMOD.2. By comparing northern to southern hemisphere ^{10}Be data to existing paleomagnetic models it could improve them. To accomplish this, I will first attempt to isolate the production signal in the ^{10}Be data by removing potential climate induced variations. I will then use various filters to remove variations in production rates on the relatively shorter, centennial to decadal, time scales associated with the sun. Discounting the effect of the climate has over ^{10}Be deposition and removing the effect of solar variations on ^{10}Be production this study is only interested in studying magnetic field variations (specifically the hemispheric differences) which is represented on longer timescales (Muscheler et al., 2016). The research questions are:

* Is ^{10}Be data of high enough quality to be utilized in studying asymmetries in the paleomagnetic field?
* Can these data be used to evaluate current magnetic field models over Laschamps?

2 Background

2.1 Cosmogenic radionuclides

2.1.1 Cosmic rays

Cosmic rays are high energy particles primarily composed of protons and α-particles. Evidence suggests that cosmic rays originate from supernovas in our galaxy, hence the name galactic cosmic rays (GCR) (Simpson, 1983). The extent of GCRs reaching our solar system, and in turn the Earth is modulated by various factors including solar modulation, geomagnetic shielding, and the energy of the rays (Muscheler, 2013).

Solar modulation refers to the suns shielding effect on GCRs, causing a deflection of low energy cosmic rays. The shielding effect of the sun is due to the heliospheric magnetic field, which is carried by the solar wind from the sun (Muscheler, 2013; Potgieter, 2013). The effect of solar modulation varies depending on the strength of solar activity, which can be observed by the number of sunspots. Lower solar activity implies a
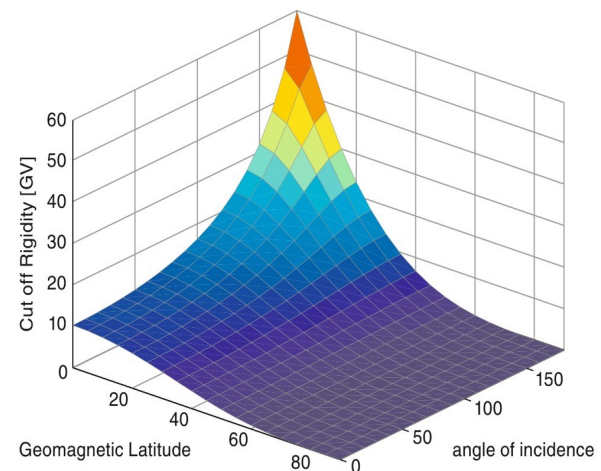

Fig. 1. Cut-off rigidity for cosmic rays on earth corresponding to the angle of incidence and the geomagnetic latitude from (Beer et al., 2011)
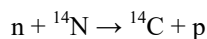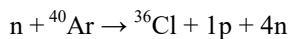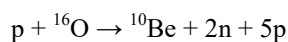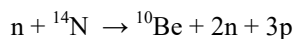
weaker heliospheric magnetic field which in turn allows for more GCRs to reach the earth.

Upon reaching Earth, cosmic rays are deflected by Earth's magnetic field, which is referred to as the geomagnetic shielding effect (GSE). The GSE is proportional to strength of the Earth's magnetic field (Muscheler, 2013), i.e. a stronger magnetic field will lead to less GCRs reaching the Earth. The effectiveness of the geomagnetic shield and consequently the number of cosmic rays that can reach Earth's atmosphere at a given location is typically defined as the cut-off rigidity (Shea & Smart, 2004). The cut-off rigidity varies depending on the morphology of Earth's largely dipolar magnetic field, and is therefore mostly latitudinally dependent, e.g. a weaker GSE in the poles due to vertical field lines (Fig. 1) (Masarik & Beer, 1999). Cosmic rays can also be created by the Sun known as solar cosmic rays. Solar cosmic rays are produced in large amounts during solar proton events where the Sun ejects particles, which reaches the Earth along the heliospheric magnetic field lines (Muscheler, 2013; Paleari et al., 2022).

2.1.2 Cosmogenic Radionuclides production

Cosmic rays with a rigidity (connected to the particle energy) above the cut-off rigidity, i.e. able to penetrate GSE are known as primary cosmic rays (Beer et al., 2011). Cosmic rays of galactic origin make up most primary cosmic rays due to the low energy in solar protons compared to GCRs, thus only accounting for a small increase in the total cosmogenic radionuclide production rate e.g. 1-2% of total ^{10}Be production (Usoskin et al., 2006).

When entering Earth's atmosphere, primary cosmic rays induce a cascade of reactions during collisions with atomic nuclei, leading to the production of cosmogenic radionuclides for e.g.

$$n + {}^{14}N \rightarrow {}^{10}Be + 2n + 3p$$

$$p + {}^{16}O \rightarrow {}^{10}Be + 2n + 5p$$

$$n + {}^{40}Ar \rightarrow {}^{36}Cl + 1p + 4n$$

$$n + {}^{14}N \rightarrow {}^{14}C + p$$

During this process secondary cosmic rays are created that continuously interact with particles in the atmosphere until the kinetic energy is dissipated (Beer et al., 2011). These secondary cosmic rays through spallation or thermal capture can produce cosmogenic radionuclides (see Fig. 2) (Muscheler, 2013). Like most cosmogenic radionuclides ^{10}Be forms in the stratosphere and the troposphere (the lowermost regions of the atmosphere) mainly through spallation with oxygen and nitrogen (Beer et al., 2011).
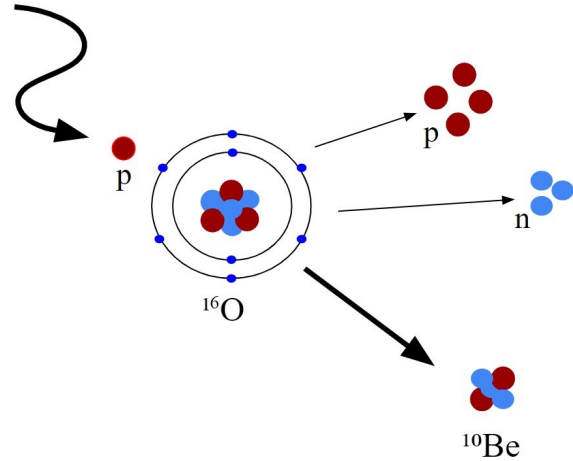

Fig. 2. Spallation of ^{16}O into ^{10}Be through one proton expelling four protons and three neutrons resulting in a ^{10}Be nucleus.

2.1.2 Cosmogenic Radionuclides Transport and Deposition

The chemical properties of cosmogenic radionuclides determine different factors including the residence time in the atmosphere, different transport ways and deposition e.g. ^{14}C and ^{36}Cl stay in there gaseous form where after ^{14}C oxidizes to ^{14}CO2 and enters the carbon cycle and ^{36}Cl either forms ^{36}Cl$_2$ or H^{36}Cl (Beer et al., 2011). The residence of cosmogenic radionuclides differs between the stratosphere and troposphere due to the stratosphere's temperature increasing with altitude, creating stable layering (Heikkilä et al., 2013). This results in cosmogenic radionuclides staying in the stratosphere ca. 0.5 - multiple years. The tropospheric residence time is limited to days or weeks due to convection cells creating more vertical transport, resulting in efficient mixing compared to the limited mixing in the stratosphere (Beer et al., 2011). While mixing in the stratosphere is less efficient, ^{10}Be in the stratosphere is still generally considered well mixed, as a result of the long residence time in atmosphere (Heikkilä et al., 2009). In I

^{10}Be after formation will attach to aerosols, residing in the atmosphere ca. 1-year on average before deposition (Muscheler, 2013). In the atmosphere ^{10}Be will eventually be scavenged through different processes such as gravitational settling, wet and dry deposition. Gravitational settling refers to the process where cosmogenic nuclides e.g. ^{10}Be attached to aerosols, get deposited because of a large enough particle mass, which primarily happens in the stratosphere due to the stable nature. Wet deposition is the biggest contributor in scavenging and refers to deposition with snow or rain. During wet deposition water droplets will collide and absorb aerosols with ^{10}Be attached, i.e. more wet deposition goes together with higher ^{10}Be deposition fluxes, since wet deposition is common in wet areas this means higher concentrations in equatori-
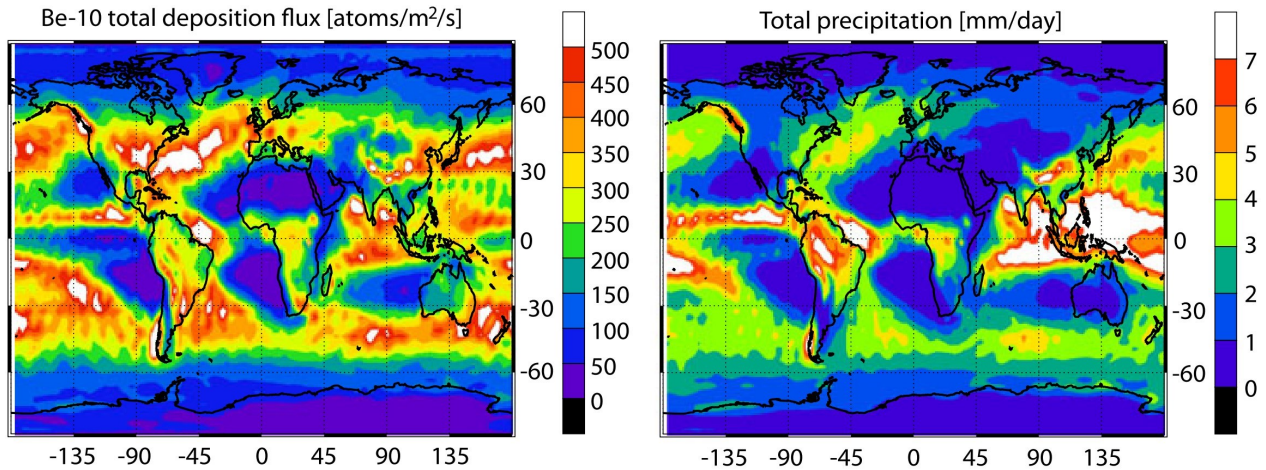
Fig. 3. Cut-off rigidity for cosmic rays on earth corresponding to the angle of incidence and the geomagnetic latitude from (Beer et al., 2011)

al latitudes (Fig. 3) (Beer et al., 2011; Muscheler, 2013). Dry deposition refers to airborne particles sticking to surfaces such as vegetation or soil and is common in dry regions hence the name. Models indicate that polar archives include ca. 60-64% of ^{10}Be originating from the stratosphere, 36-40% from the troposphere. 16% of the tropospheric signal can be traced to mid - southern latitudes and 20% from tropospheric Polar Regions i.e. the polar caps (Beer et al., 2011).

2.2 Geomagnetic Field
2.2.1 Basics
Earth's magnetic field is generated by the fluid motion of earth's liquid outer core, this process is known as the geodynamo (Landeau et al., 2022). This generated magnetic field approximates a dipole dominated field, reminiscent of a traditional magnet with a magnetic north and south (Beer et al., 2011). Dipole dominated fields as seen today can generally be approximated to constitute for 90% of Earth's surface field.

The magnetic field is often represented with field lines flowing from within the Earth. The angle between the field lines and Earth's surface is known as the inclination, whereas the angle between the magnetic field's horizontal component and geographic north is known as declination. These properties of the magnetic field together constitute the direction of Earth's magnetic field (Fig. 4).

Over geological time the magnetic fields strength and direction has varied and shows e.g. excursion and reversal events. Variations on timescales between 1 to 10^5 years (primarily between 10^3 to 10^4 years) are known as geomagnetic secular variations. Geomagnetic secular variations are non-cyclical, created by fluctuations from dipole dominated fields during long time periods and fluctuations from non-dipole fields during shorter periods (Butler, 1992).

Extreme secular variations such as reversals and excursions are marked by a weakening magnetic field,

where reversals are noted with a flip in polarity and excursions are marked by a return. During such events the dipole dominated field disappears making the non-dipole field relatively more important. Important to this study is the excursion of Laschamps ca. 41 000 years ago, representing the second most recent excursion after Mono Lake (Brown et al., 2018).

2.2.2 Paleomagnetic data
Data of the paleomagnetic field, in addition to cosmogenic radionuclides can also be preserved in geological

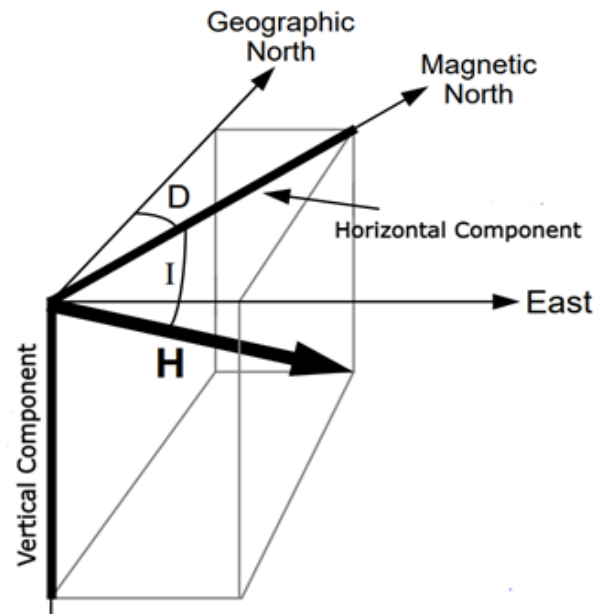*Fig. 4.* The directions of the magnetic field showing the horizontal component and the vertical component. The angle between the geographic north and the horizontal component is defined as declination (*D*), whereas the angle between the total magnetic field vector known as (**H**), comprising both the horizontal and vertical component and the magnetic north is known as inclination (*I*). The figure is adapted from (Butler, 1992).

9

materials (sediments, rocks) and archaeological materials. This is attributed to materials containing iron oxides, for instance the mineral magnetite (Fe3O4) which exhibits magnetic properties used for proxy studies (Dunlop, 1995). During crystallization magnetic minerals will magnetize, aligning with the present magnetic field thus resulting in preservation of the paleomagnetic field, this is known as natural remanent magnetization. (Beamud, n.d.). Despite the possibility to study the magnetic field in geological materials, there is a distinct lack of paleomagnetic data from the southern hemisphere, central Asia and higher latitudes which complicates modelling of the paleomagnetic field (Korte et al., 2019).

3. Methods
3.1 Sources and data
Public literature was primarily collected from databases: Web of Science, Scopus and LUBsearch. Common search terms included: "Laschamps", "geomagnetic field", "GCR" and "atmospheric ^{10}Be". The ^{10}Be ice core data utilized in this study are published in Muscheler et al., (2004) and Raisbeck et al. (2017). Ice core data from Greenland featuring (GRIP) and (NGRIP) were each taken from Muscheler et al., (2004) for GRIP and Raisbeck et al. (2017) for NGRIP. Vostok, "EPICA DomeC" (EDC) and "EPICA Dronning Maud Land" (EDML) originate from Antarctica (see Fig. 5) (Raisbeck et al., 2017). From sites EDC and Vostok, dD(‰) is included as a climate proxy, compared to EDML, GRIP and NGRIP which utilize δ^{18}O (‰). ^{10}Be flux data is also provided in all data sites, reflecting data corrected for snow accumulation (Jouzel, 2013; Raisbeck et al., 2017).

3.2 ^{10}Be production reconstructions
Attempts were made to use climate proxy's dD and δ^{18}O to remove potential climate influences in the ^{10}Be concentration data. First, dD or δ^{18}O data, were plotted against ^{10}Be concentrations in so called scatter plots (see Fig. 6C). An exponential trend line was fitted and based on this trend line. The function of the exponential trendline termed ($f(x)$), depicting ^{10}Be as a function of dD/ δ^{18}O, where dD or δ^{18}O are expressed as (x). Utilizing the $f(x)$, corrected data were created in two ways. First, corrected data were created as a difference between ^{10}Be concentration data and $f(x)$, i.e. *corrected data = ^{10}Be – f(x)*. Furthermore, corrected data was created as a quotient of ^{10}Be concentration data and $f(x)$, i.e. *corrected data = ^{10}Be/f(x)*. The corrected data were then low pass filtered (cut off frequency 1/600yrs), due to magnetic field variations dominating during longer timescales (see Fig. 8) (Nilsson et al., 2022). The filtering was done by calculating a mean value of 60 data points, for reference 1 data point is equal to 10 years.

Flux data is created as a product between ^{10}Be concentration data and snow accumulation rate, i.e. *Flux = ^{10}Be * mass accumulation rate (*g cm^{-2} year^{-1}) (see Fig. 7). After this flux data was normalised, calculated as a quotient of the mean ^{10}Be flux, i.e. *normalised flux = datapoint/mean*. Lastly, flux data were low pass fil-

tered (cut off frequency 1/600yrs) calculated as a mean of 60 data point with each data point corresponding to 10 years. After all data were corrected and filtered a stack would be calculated for Greenland and Antarctica (see Fig. 9). The stacks were calculated as mean of the filtered data e.g. *(GRIP + NGRIP)/2*. The stacked data were compared to LSMOD.2 predictions of production rates (assuming a constant solar modulation). First the Greenland stack, representing the northern hemisphere production rates (Q_{NH}) was compared to northern LSMOD.2 data. After this the Antarctica stack, representing the southern hemisphere production rates (Q_{SH}) was compared to southern LSMOD.2 data. During the comparisons, data could be interpreted in different ways depending on the position of models relative to each other. To compare data, we again normalised data at (41.95 ka) and at (40.55 ka) (see Fig. 10). This is achieved by dividing the flux data by the ^{10}Be flux at (41.95 or 40.55 ka) and multiplying by the production rates predicted by LSMOD.2 at the same time (41.95 or 40.55 ka) e.g. normalising data at 40.55 ka for the northern hemisphere assumes the amount of ^{10}Be being deposited at the ice during this time point corresponds to the average production rates for LSMOD.2 at the same time. After the hemispherical comparison, global ^{10}Be data (Q_{GL}), representing a mean of Q_{NH} and Q_{SH} were calculated. Calculated Q_{GL} were then compared to global LSMOD.2 data where Q_{GL} is defined as

$$Q_{GL} = \frac{(Q_{NH} + Q_{SH})}{2}$$

Lastly hemispherical production asymmetry (HPA) was calculated for ^{10}Be data, LSMOD.2 and other magnetic field models such as GGF100k and GGFS720. Calculated HPA can be expressed as (Nilsson et al., 2024).

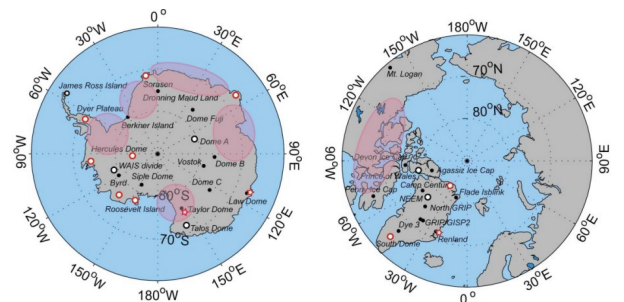$$HPA = \frac{(Q_{NH} - Q_{SH})}{Q_{GL}}$$

Fig. 5. Locations of ice core drilling sites from Antarctica (left panel) and Greenland (right panel) (Jouzel, 2013).
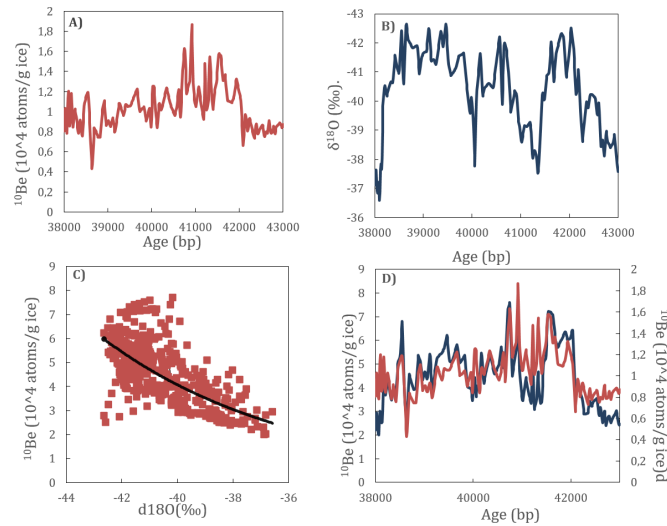
10

Fig. 6. Process of correcting GRIP ^{10}Be concentration data with climate proxies, in this case δ^{18}O represents the climate proxy shown. A) Production rates for ^{10}Be concentration without correction. B) δ^{18}O representing the climate proxy which will be corrected for. C) ^{10}Be concentration data as a function of δ^{18}O. The *f(x)* represents a exponential trendline *Y = 0,0122e$^{-0.145x}$* where δ^{18}O is expressed as (*x*). D) ^{10}Be concentration data (blue) plotted against correct-
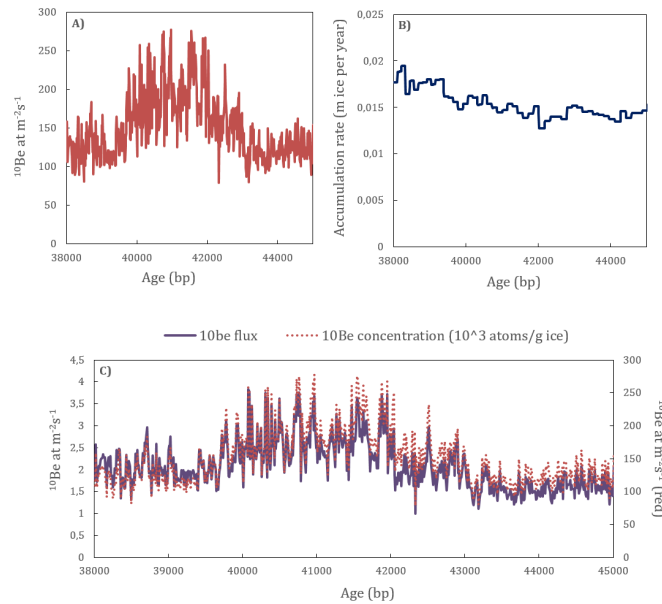
Fig. 7. Three time-based graphs from EDC showing ^{10}Be concentration data corrected for snow accumulation, creating ^{10}Be flux data. A) ^{10}Be concentration before correction. B) Snow accumulation (m ice per year). C) ^{10}Be flux (purple) corrected for snow accumulation compared with the original ^{10}Be concentration (dotted red).
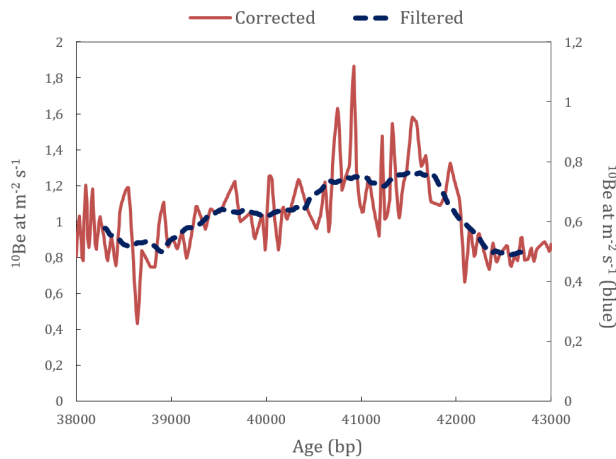
Fig. 8. Corrected production rates for ^{10}Be concentration data (red) plotted against low pass filtered (cut off frequency 1/600yrs) ^{10}Be concentration data (dotted blue). Dataset is taken from GRIP.

11

4 Results

Here the results presented showcase detailed comparisons between [10]Be flux data (from Raisbeck et al. (2017) and Muscheler et al., (2004)) termed "synchronized data" and LSMOD.2 in three categories, hemispherical, global data, and hemispherical produ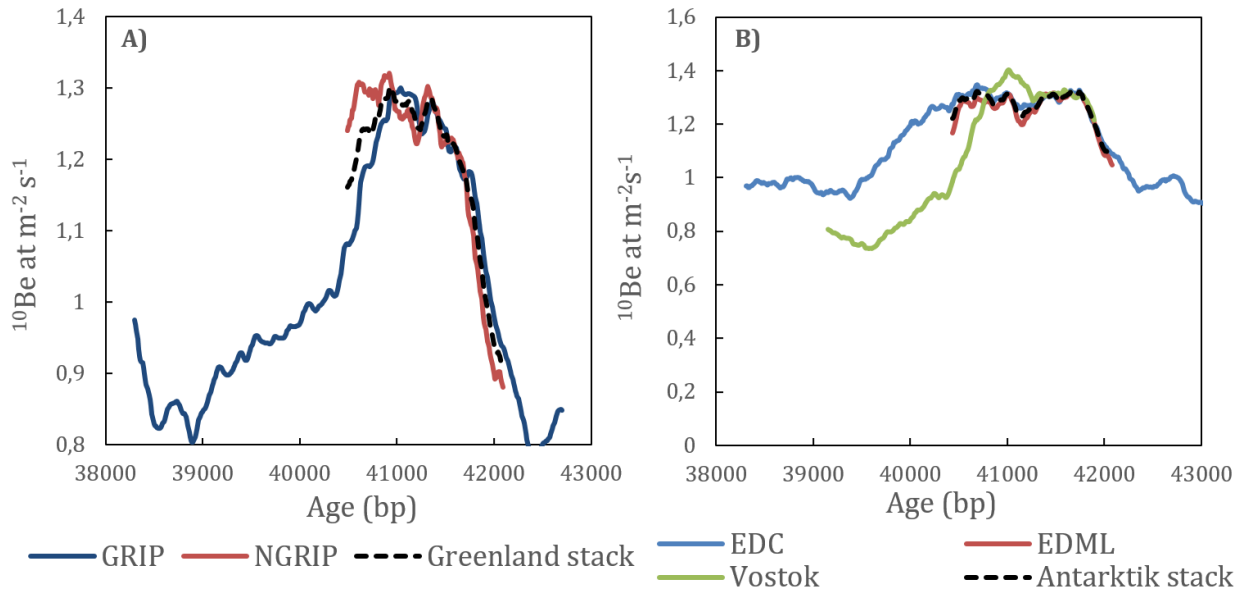ction asymmetry. Since [10]Be concentration data, even after correction showed climate influence, we instead only present corrected and filtered data for [10]Be flux. During these comparisons, results presented in the figures will primarily be shown for data normalised at 40.55 ka. Lastly synchronized [10]Be flux will be compared with other magnetic field models to evaluate the best fit. The results are presented in 6 graphs, showcasing age (bp) on the x axis and [10]Be production rates on the y axis.

4.1 LSMOD.2

Figure 10 shows two time-based reconstructions of hemispherical [10]Be flux from Raisbeck et al. (2017) and Muscheler et al., (2004) compared with LSMOD.2 normalised at 40.55 ka. In the [10]Be Antarctica stack Vostok was excluded, only utilizing EDC and EDML (see Fig. 7B). The northern hemisphere comparison between stacked normalised (40.55 ka) and LSMOD.2 show good agreement during 40.5 and 41.25 ka. During this interval both stacked data and LSMOD.2 display high average hemispherical [10]Be production rates, ranging between 0.06 and 0.07 (atoms/m2/s), in contrast stacked data shows slightly lower production rates. In comparison, stacked data, normalised (41.95 ka) shows a worse agreement from 40.5 and 41.25 ka. Instead, the results show a good agreement from 41.3 to 42 ka.

In the southern hemisphere comparison between Antarctic stacked data and LSMOD.2, shown in Figure 8B, an agreement is seen in production rates for stacked data normalised (40.55 ka) and LSMOD.2 between 40.5 and 41.25 ka, with production rates varying around ~0.07 (atoms/m2/s). In this interval,
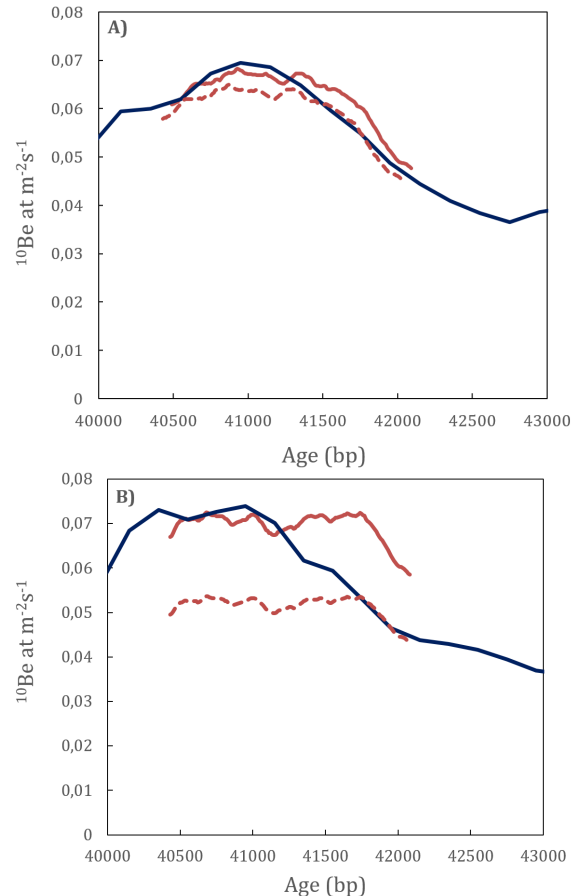
Fig. 10. Two reconstructions of hemispherical [10]Be production/flux. A) Northern hemispherical production rates of LSMOD.2 (blue), compared with synchronized data normalized at 40.55 ka (red) and synchronized data normalized at 41.95 ka (dotted red). B) Southern hemispherical production rates of LSMOD.2 (blue), compared with synchronized data normalized at 40.55 ka (red) and synchronized data normalized at 41.95 ka (dotted red).

stacked data closely follows LSMOD.2 only showing slightly lower production rates ca. 0.001 atoms/m2/s then LSMOD.2. This is seen more noticeable between 40.7 and 41.2 ka. In comparison, stacked normalised Q_{SH} (41.95 ka) shows a weak agreement with LSMOD.2 between 40.5 and 41.75 ka, having production rates 0.02 (atoms/m2/s) lower. Although a strong agreement can be seen between 41.75 to 42 ka. Comparing normalised Q_{NH} (40.55 ka) and normalised Q_{SH} (40.55 ka) shows similar production rates with each other and to LSMOD.2 between 40.5 and 41.25 ka. Both show a drop in production rates after this point where Q_{NH} drops earlier around 41.5 ka whereas Q_{SH} shows lower production rates after 41.75 ka.

4.1.2 Global data

Figure 11 displays a time-based global reconstruction of ^{10}Be flux, calculated from Raisbeck et al. (2017) and Muscheler et al., (2004) compared with LSMOD.2. The comparison between synchronized Q_{GL} and LSMOD.2 global data shows a general good agreement from 40.5 to 41.25 ka. During this interval both Q_{GL} and LSMOD.2 display high ^{10}Be production rates, peaking roughly at the start of the excursion 41 ka. After 41.25 ka LSMOD.2 starts to decline to high average production rates. On the other hand, Q_{GL} remains with high production rates ca. 0.01 (atoms/m2/s) higher, only declining at a similar trend as LSMOD.2 after ~41.75 ka. In Figure 7 we can note a similar development in production rates for synchronized data as in figure 9, showcasing high production rates between 40.5 to 41.75 ka, peaking ~41 ka and sharply dropping after 41.75 ka.

4.1.3 Hemispherical production asymmetry

Figure 10 presents a time-based reconstruction of

calculated HPA compared with LSMOD.2. Comparing normalised HPA (40.55 ka) shows a similar trend from 40.5 to 41.2 ka. Furthermore, synchronized data between 40.5 to 40.7 ka starts to show centennial fluctuations with frequencies in the range of ca. 200 years. These occur throughout the whole investigated period from 40.5 to 42.1 ka for synchronized data normalised both 40.55 and 41.95 ka and are most notable between 40.5 to 41.5 ka. Peak production rates for synchronized data are visible at 41.1 ka. In contrast LSMOD.2 shows several peaks in production rates during three intervals, between 41.3 and 41.4 ka, ~42 ka and at 43 ka. Synchronized HPA normalised (41.95 ka) shows large positive asymmetries between 40.5 and ~41.8 ka. The productions rates show ~0.2 higher production rates, peaking ~41 ka. Only between 41.8 and 42 ka the production rates return to similar levels as LSMOD.2.

4.2 Comparison with other magnetic field models

Figure 13 shows a comparison between calculated hemispherical asymmetry production synchronized data compared with three reconstructions being LSMOD.2, (GGFS720) and (GGF100k), investigating the best fit for calculated synchronized HPA. Note that only the ^{10}Be data show fluctuations of ~200 years. During the last thousand years, ending from 40.5 ka LSMOD.2 we observe the best agreement, where GGFS720 differs the most with low ^{10}Be production rates. On the other hand, GGF100k shows overall higher ^{10}Be production rates, ~0.15 (atoms/m2/s) higher during the first 500 years. From 41 to ~41.7 ka a general agreement between GGF100k and synchronized data is shown. On the other
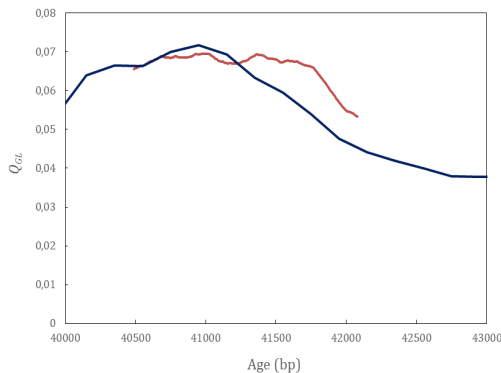

Fig. 11. Global reconstruction of the paleomagnetic field. Global stack of data from Raisbeck et al. (2017) is shown in red and global data from LSMOD.2 is shown in blue. The red data utilizes ^{10}Be flux from ice cores whereas the blue data is based on remanent magnetisation measurements that were used for creating a global geomagnetic field model.
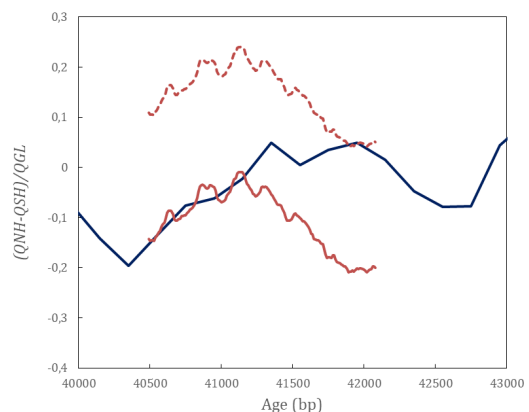

Fig. 12. Hemispherical production asymmetry defined as $(Q_{NH}-Q_{SH})/Q_{GL}$ showed for synchronized data normalized at 40.55 ka (red), synchronized data normalized at 41.95 ka (dotted red) compared with LSMOD.2 (blue).

hand, GGFS70 shows large asymmetries compared to synchronized data, leading to high calculated [10]Be production rates between 41.5 to 42 ka where at the same time synchronized data shows low [10]Be production. Due to these big disparities between synchronized and GGFS720 hemispherical asymmetry production, further evaluation will instead only consider LSMOD.2 and GGF100k.

Normalised data at 40.55 and 41.95 ka for GGF100k yielded no good fit for synchronized data, only showing a slightly better fit compared to synchronized data normalised (40.55 ka). LSMOD.2 differs from GGF100k, where LSMOD.2 shows a similar trend between 40.5 to 41.2 ka with synchronized data, contrasted to GGF100k which shows a similar trend with synchronized data after 41.2 ka to 41.7 ka, meaning GGF100k and LSMOD.2 are inverse to a degree. Furthermore, LSMOD.2 shows a longer agreement between synchronized data roughly 700 years compared with GGF100k ca. 500 years. In general, LSMOD.2 shows more similar 10Be production rates to LSMOD.2 compared with GGF100k which only shows similar production rates at ~40.7 ka to 42 ka.

5 Discussion

5.1 Geomagnetic field model agreement

As seen in figure 10A there is a good agreement in production rates between normalised data (40.55 ka) and LSMOD.2 from 40.5 ka and 41.25 ka, weakening from 41.25 to 42 ka. Normalised data (41.95 ka) presents similar results to normalised data (40.55 ka) and LSMOD.2, only showing slightly more agreement between 41.25 and 42 ka and less agreement between 40.5 and 41.25 ka with LSMOD.2. As a result of both Q_{NH} data normalised (40.55 and 41.95 ka) being like each other and LSMOD.2, [10]Be data robustness shows promise for magnetic field reconstructions over the northern hemisphere.

The southern hemisphere results presented in figure 8B show a general agreement between normalised data (40.55 ka) and LSMOD.2 from 40.5 and 41.75 ka. However, normalised data (41.95 ka) shows a reverse trend compared with data normalised (40.55 ka) with low production rates from 40.5 and 41.75 ka, showing good agreements from 41.75 to 42 ka with LSMOD.2. In addition to being dissimilar to normalised data (40.55 ka), there is an overall weak agreement with LSMOD.2. Due to normalised data (41.95 ka) diverging with normalised data (40.55 ka) and LSMOD.2 this could point to a southern hemisphere problem.

Comparing Q_{NH} with Q_{SH} shows a similar trend where normalised data (40.55 ka) corresponds well with LSMOD.2 in the beginning and slightly worse (>41.25 ka). Moreover, Q_{NH} and Q_{SH} normalised (41.95 ka) also shows a similar trend with each other where the production rates are reversed compared to normalised data (40.55 ka) i.e. slightly less agreement in the beginning and a better fit to LSMOD.2 (>~41.75 ka).
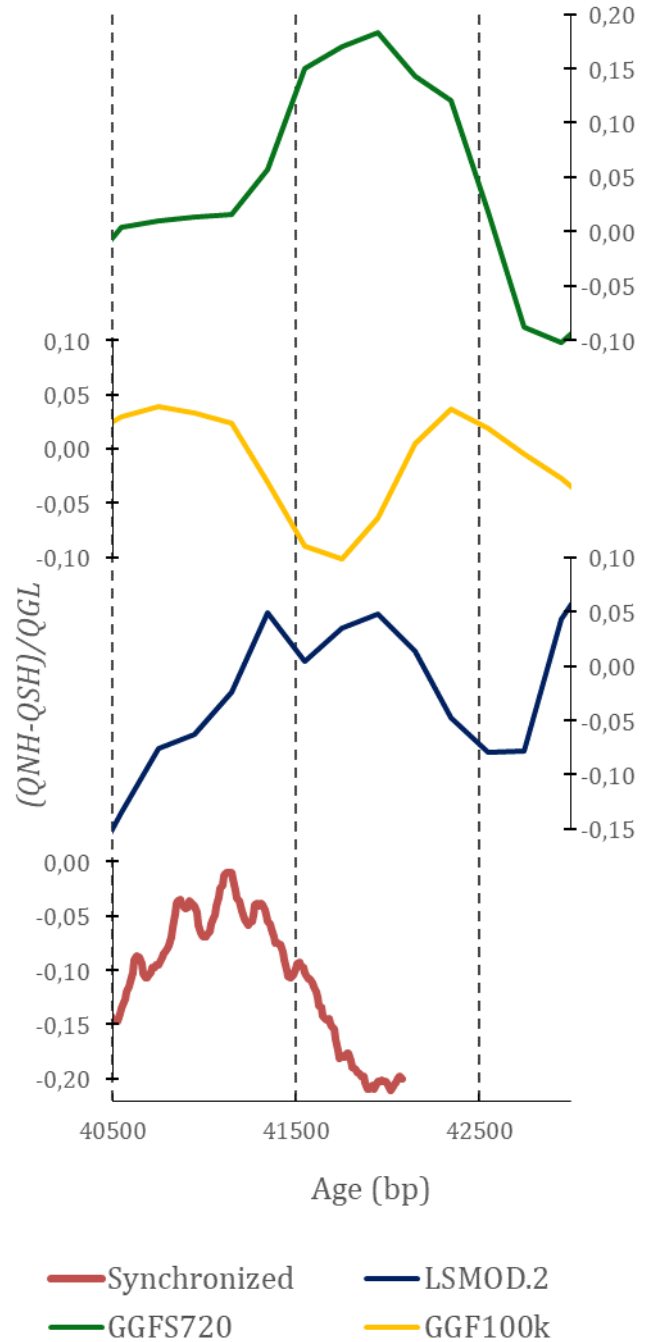
Fig. 13. Four independent reconstructions of the paleomagnetic field, calculated from HPA derived from Andreas et al., (2024). Synchronized data normalized (40.55 ka) is shown in red, LSMOD.2 in blue, GGF100k in yellow and GGFS720 in green. The x axis shows [10]Be production on a relative scale.

Note that while Q_{NH} and Q_{SH} normalised at 41.95 ka does show similar trends as mentioned above, Q_{SH} varies considerably in overall production rates with Q_{NH} and LSMOD.2 thus showing bad agreements with both even though they share a similar trend. Overall Q_{NH} normalised at both 40.55 ka and 41.95 ka show a relatively good

14

agreement with each other. Q_{NH} normalised (40.55 and 41.95 ka) also shows a good agreement with LSMOD.2 and Q_{SH} normalised (40.55 ka).

5.2 Uncertainties in reconstructions

Filtered [10]Be concentration data from Raisbeck et al. (2017) and Muscheler et al. (2004) were shown to be unreliable even after correction, thus not being utilized in the results. This could be due to the way corrected [10]Be data was created. In this study we first calculated corrected data as a difference between [10]Be concentration data and $f(x)$ mentioned above. However, during comparisons between e.g. EDC, EDML and Vostok there was no clear correlation i.e. only usable to asses' local [10]Be deposition. Because of this we calculated corrected [10]Be data as a quotient of [10]Be concentration data and $f(x)$ mentioned above. Nevertheless, this didn't provide any noteworthy results for [10]Be concentration data during comparisons with other data series; thus, flux data was preferred over [10]Be concentration data.

Another possibility to isolate magnetic field signals in [10]Be concentration data is larger mean in filtering i.e. stronger low pass filter. Because of this the results suggest solar induced variations as e.g. 200 years cyclicity are seen as fluctuations with small peaks and valleys (Fig. 9). A stronger low pass filter would reflect magnetic field changes more accurately. Nevertheless, increasing the filter above 600 years would not affect the overall results presented due to the focus being on long term variations, which are visible with or without the 200-year solar cyclicity.

Different results are also presented depending on how data is normalised. If we use figure 10 as an example, normalising at 41.95 ka gives maximum asymmetries during the Laschamps excursion, compared to data normalised at 40.55 ka resulting in maximum asymmetries in the beginning of the excursion. Nevertheless, since the asymmetries presented are shown in relative measurements, this implies that we can only investigate how reliable LSMOD.2 is compared with [10]Be data, and not when we have maximum asymmetries. Because of this we cannot claim when LSMOD.2 is the most reliable due to the results being relative.

5.3 Analysis of magnetic field models

Comparing synchronized HPA with LSMOD.2, GGF100k and GGFS720 shows a weak agreement with GGFS720, only displaying some correlation with GGF100k and LSMOD.2. While GGF100k had a better agreement between 41.2 and 41.7 ka LSMOD.2 showed a longer agreement between 40.5 and 41.2 ka. Normalised data at 41.95 ka led to no improvement for GGF100k. Due to this, LSMOD.2 can be considered the best fit for synchronized data. However, since none of the above-mentioned models show any general agreement with each other it can thus be argued that [10]Be data could still prove useful.

As seen in figure 12, synchronized [10]Be data can be interpreted in two different ways during comparisons with LSMOD.2 depending on the normalisation point (40.55 or 41.95 ka). Normalising at 40.55 ka results in a large negative asymmetry between 41.2 and 42 ka. Moreover, normalising at 41.95 ka gives a positive asymmetry during the excursion. Positive asymmetries imply a weak magnetic field for the northern hemisphere due to high production rates implying lower cut off rigidities which in turn indicates a weaker GSE. This also applies to the southern hemisphere with negative asymmetries being linked to a stronger GSE.

6 Conclusion

To summarize, [10]Be flux data over the northern hemisphere showed good agreement with LSMOD.2 for both normalised datasets (40.55 and 41.95 ka). In contrast, the [10]Be data over the southern hemisphere differed between normalised datasets (40.55 and 41.95 ka), pointing to weak robustness in southern hemisphere [10]Be data. In the comparison between different magnetic field models, LSMOD.2 showed the longest agreement, in contrast to GGFS720 being the worst fit for [10]Be data. The agreement between LSMOD.2 and [10]Be data were strongest from 40.5 to 41.2 ka. Nevertheless, the overall agreement between [10]Be data and magnetic field models such as LSMOD.2 were relatively weak, only showing limited use as an independent signal reflecting local [10]Be deposition in the northern hemisphere.

7 Acknowledgements

8 References

Beamud, E. (n.d.). Paleomagnetism: principles and applications. Retrieved April 9, 2024, from https://diposit.ub.edu/dspace/bitstream/2445/32163/1/MT08%20-%20Paleo-magnetism%20_ed2.pdf

Beer, J., McCracken, K. G., & Steiger, R. v. (2011). *Cosmogenic radionuclides. theory and applications in the terrestrial and space environments* [Bibliographies Online Non-fiction Electronic document]. Springer. https://ludwig.lub.lu.se/login?url=https://search.ebscohost.com/login.aspx?direct=true&AuthType=ip,uid&db=cat02271a&AN=atoz.ebs1160764e&site=eds-live&scope=site http://search.ebscohost.com/login.aspx?direct=true&site=edspub-live&scope=site&type=44&db=edspub&authtype=ip,guest&custid=s3912429&groupid=main&profile=eds&bquery=AN%201160764

Brown, M., Korte, M., Holme, R., Wardinski, I., & Gunnarson, S. (2018). Earth's magnetic field is probably not reversing [research-article]. *Proceedings of the National Academy of Sciences of the United States of America*, *115*(20), 5111-5116. https://ludwig.lub.lu.se/login?url=https://search.ebscohost.com/login.aspx?direct=true&AuthType=ip,uid&db=edsjsr&AN=edsjsr.26509492&site=eds-live&scope=sitehttps://www.ncbi.nlm.nih.gov/pmc/articles/PMC5960311/pdf/pnas.201722110.pdf

Heikkilä, U., Beer, J., Abreu, J. A., & Steinhilber, F. (2013). On the Atmospheric Transport and Deposition of the Cosmogenic Radionuclides (10Be): A Review. *Space Science Reviews*, *176*(1), 321-332. https://doi.org/10.1007/s11214-011-9838-0

Heikkilä, U., Beer, J., & Feichter, J. (2009). Meridional transport and deposition of atmospheric 10Be. *Atmospheric Chemistry and Physics*, *9*(2), 515-527. https://doi.org/10.5194/acp-9-515-2009

Jouzel, J. (2013). A brief history of ice core science over the last 50 yr. *Climate of the Past*, *9*(6), 2525-2547. https://doi.org/10.5194/cp-9-2525-2013

Masarik, J., & Beer, J. (1999). Simulation of particle fluxes and cosmogenic nuclide production in the Earth's atmosphere. *Journal of Geophysical Research. Atmospheres*, *104*(D10), 12099-12111. https://doi.org/10.1029/1998JD200091

Muscheler, R. (2013). *10Be and Cosmogenic Radionuclides in Ice Cores* (Vol. 2) [Topic overview]. Elsevier, Inc. https://ludwig.lub.lu.se/login?url=https://search.ebscohost.com/login.aspx?direct=true&AuthType=ip,uid&db=edsgvr&AN=edsgcl.3164400164&site=eds-live&scope=site

Muscheler, R., Adolphi, F., Herbst, K., & Nilsson, A. (2016). The Revised Sunspot Record in Comparison to Cosmogenic Radionuclide-Based Solar Activity Reconstructions. *Solar Physics*, *291*(9-10), 3025-3043. https://doi.org/10.1007/s11207-016-0969-z

Muscheler, R., Beer, J., Wagner, G., Laj, C., Kissel, C., Raisbeck, G. M., Yiou, F., & Kubik, P. W. (2004). Changes in the carbon cycle during the last deglaciation as indicated by the comparison of 10Be and 14C records. *Earth and Planetary Science Letters*, *219*(3-4), 325-340. https://doi.org/10.1016/s0012-821x(03)00722-2

Nilsson, A., Suttie, N., Stoner, J. S., & Muscheler, R. (2022). Recurrent ancient geomagnetic field anomalies shed light on future evolution of the South Atlantic Anomaly. *Proceedings of the National Academy of Sciences of the United States of America*, *119*(24), Article e2200749119. https://doi.org/10.1073/pnas.2200749119

Panovska, S., Poluianov, S., Gao, J. W., Korte, M., Mishev, A., Shprits, Y. Y., & Usoskin, I. (2023). Effects of Global Geomagnetic Field Variations Over the Past 100,000 Years on Cosmogenic Radionuclide Production Rates in the Earth's Atmosphere. *Journal of Geophysical Research-Space Physics*, *128*(8), Article e2022JA031158. https://doi.org/10.1029/2022ja031158

Potgieter, M. S. (2013). Solar Modulation of Cosmic Rays. *Living Reviews in Solar Physics*, *10*(3), 5-+. https://doi.org/10.12942/lrsp-2013-3

Raisbeck, G. M., Cauquoin, A., Jouzel, J., Landais, A., Petit, J. R., Lipenkov, V. Y., Beer, J., Synal, H. A., Oerter, H., Johnsen, S. J., Steffensen, J. P., Svensson, A., & Yiou, F. (2017). An improved north-south synchronization of ice core records around the 41 kyr 10Be peak. *Climate of the Past*, *13*(3), 217-229. https://doi.org/10.5194/cp-13-217-2017

Shea, M. A., & Smart, D. F. (2004). Preliminary study of cosmic rays, geomagnetic field changes and possible climate changes. In J. M. Pap, J. Kuhn, K. Labitzke, & M. A. Shea (Eds.), *Solar Variability and Climate Change* (Vol. 34, pp. 420-425). https://doi.org/10.1016/j.asr.2004.02.008

Usoskin, I. G., Solanki, S. K., Kovaltsov, G. A., Beer, J., & Kromer, B. (2006). Solar proton events in cosmogenic isotope data. *Geophysical Research Letters*, *33*(8), Article L08107. https://doi.org/10.1029/2006gl026059

Tidigare skrifter i serien "Examensarbeten i Geologi vid Lunds universitet":

630. Neumann, Daniel, 2022: En mosasaurie (Reptilia, Mosasauridae) av paleocensk ålder? (15 hp)
631. Svensson, David, 2022: Geofysisk och geologisk tolkning av kritskollors utbredning i Ystadsområdet. (15 hp)
632. Allison, Edward, 2022: Avsättning av Black Carbon i sediment från Odensjön, södra Sverige. (15 hp)
633. Jirdén, Elin, 2022: OSL dating of the Mesolithic site Nilsvikdalen 7, Bjorøy, Norway. (45 hp)
634. Wong, Danny, 2022: GIS-analys av effekten vid stormflod/havsnivåhöjning, Morupstrakten, Halland. (15 hp)
635. Lycke, Björn, 2022: Mikroplast i vattenavsatta sediment. (15 hp)
636. Schönherr, Lara, 2022: Grön fältspat i Varbergskomplexet. (15 hp)
637. Funck, Pontus, 2022: Granens ankomst och etablering i Skandinavien under postglacial tid. (15 hp)
638. Brotzen, Olga M., 2022: Geologiska besöksmål och geoparker som plattform för popularisering av geovetenskap. (15 hp)
639. Lodi, Giulia, 2022: A study of carbon, nitrogen, and biogenic silica concentrations in *Cyperus papyrus*, the sedge dominating the permanent swamp of the Okavango Delta, Botswana, Africa. (45 hp)
640. Nilsson, Sebastian, 2022: PFAS- En sammanfattning av ny forskning, med ett fokus på föroreningskällor, provtagning, analysmetoder och saneringsmetoder. (15 hp)
641. Jägfeldt, Hans, 2022: Molnens påverkan på jordens strålningsbalans och klimatsystem. (15 hp)
642. Sundberg, Melissa, 2022: Paleontologiska egenskaper och syreisotopsutveckling i borrkärnan Limhamn-2018: Kopplingar till klimatförändringar under yngre krita. (15 hp)
643. Bjermo, Tim, 2022: A re-investigation of hummocky moraine formed from ice sheet decay using geomorphological and sedimentological evidence in the Vomb area, southern Sweden. (45 hp)
644. Halvarsson, Ellinor, 2022: Structural investigation of ductile deformations across the Frontal Wedge south of Lake Vättern, southern Sweden. (45 hp)
645. Brakebusch, Linus, 2022: Record of the end-Triassic mass extinction in shallow marine carbonates: the Lorüns section (Austria). (45 hp)
646. Wahlquist, Per, 2023: Stratigraphy and palaeoenvironment of the early Jurassic volcaniclastic strata at Djupadalsmölla, central Skåne, Sweden. (45 hp)
647. Gebremedhin, G. Gebreselassie, 2023: U-Pb geochronology of brittle deformation using LA-ICP-MS imaging on calcite veins. (45 hp)
648. Mroczek, Robert, 2023: Petrography of impactites from the Dellen impact structure, Sweden. (45 hp)
649. Gunnarsson, Niklas, 2023: Upper Ordovician stratigraphy of the Stora Sutarve core (Gotland, Sweden) and an assessment of the Hirnantian Isotope Carbon Excursion (HICE) in high-resolution. (45 hp)
650. Cordes, Beatrix, 2023: Vilken ny kunskap ger aDNA-analyser om vegetationsutvecklingen i Nordeuropa under och efter Weichsel-istiden? (15 hp)
651. Bonnevier Wallstedt, Ida, 2023: Palaeocolour, skin anatomy and taphonomy of a soft-tissue ichthyosaur (Reptilia, Ichthyopterygia) from the Toarcian (Lower Jurassic) of Luxembourg. (45 hp)
652. Kryffin, Isidora, 2023: Exceptionally preserved fish eyes from the Eocene Fur Formation of Denmark – implications for palaeobiology, palaeoecology and taphonomy. (45 hp)
653. Andersson, Jacob, 2023: Nedslagskratrars inverkan på Mars yt-datering. En undersökning av Mars främsta yt-dateringsmetod "Crater Counting". (15 hp)
654. Sundberg, Melissa, 2023: A study in ink – the morphology, taphonomy and phylogeny of squid-like cephalopods from the Jurassic Posidonia Shale of Germany and the first record of a loligosepiid gill. (45 hp)
655. Häggblom, Joanna, 2023: En patologisk sjölilja från silur på Gotland, Sverige. (15 hp)
656. Bergström, Tim, 2023: Hur gammal är jordens inre kärna? (15 hp)
657. Bollmark, Viveka, 2023: Ca isotope, oceanic anoxic events and the calcareous nannoplankton. (15 hp)
658. Madsen, Ariella, 2023: Polycykliska aromatiska kolväten i Hanöbuktens kustnära sediment - En sedimentologisk undersökning av vikar i närhet av pappersbruk. (15 hp)
659. Wangritthikraikul, Kannika, 2023: Holocene Environmental History of Warming Land, Northern Greenland: a study based on lake sediments. (45 hp)
660. Kurop, Anna, 2023: Reconstruction of the glacier dynamics and Holocene chronology of retreat of Helagsglaciären in Central

661. Frisendahl, Kajsa, 2023: Holocene environmental history of Washington Land, NW Greenland: a study based on lake sediments. (45 hp)

662. Ryan, Cathal, 2023: Luminescence dating of the late Quaternary loess-palaeosol sequence at Velika Vrbica, Serbia. (45 hp)

663. Lindow, Wilma, 2023: U-Pb datering av zirkon i metasediment tillhörande Stora Le-Marstrand, SV Sverige. (15 hp)

664. Bengtsson, Kaisa, 2023: Geologisk karaktärisering av den kambriska Faluddensandstenen i Östersjön och dess lämplighet för koldioxidlagring. (15 hp)

665. Granbom, Johanna, 2023: Insights into simple crater formation: The Hummeln impact structure (Småland, Sweden). (45 hp)

666. Jonsson, Axel, 2023: Datering av vulkanen Rangitoto, Nya Zeeland, genom paleomagnetiska analysmetoder. (15 hp)

667. Muller, Elsa, 2023: Response of foraminifera *Ammonia confertitesta* (T6) to ocean acidification, warming, and Deoxygenation An experimental approach. (45 hp)

668. Struzynska, Patrycja, 2023: Petrography, geochemistry, and origin of deep magmatic cumulates in the Canary Islands – the xenolith record. (45 hp)

669. Krätzer, Tobias, 2023: Artificiella torskrev i Hanöbukten: Förstudie. (15 hp)

670. Khorshidian, Farid, 2023: 3D modelling and resistivity measurements for hydrogeological assessments in the northern part of Vombsänkan. (45 hp)

671. Sundberg, Oskar, 2023: Methodology for Stored Heat "Heat In Place" (HIP) assessment of geothermal aquifers – Exemplified by a study of the Arnager Greensand in SW Scania. (45 hp)

672. Haraldsson, Emil, 2023: Kan akademin hjälpa industrin utveckla mer robusta grundvattenmodeller? En studie av moderna Svenska industriframtagna grundvattenmodeller. (15 hp)

673. Barabas, Ricky, 2024: Kan chockmetamorfos i okonventionella mineral hjälpa till att identifiera nedslagskratrar? (15 hp)

674. Nilsson, Sebastian, 2024: The glaciotectonic evolution of Ven, Sweden: insights from a comprehensive structural, sedimentological, and geomorphological analysis. (45 hp)

675. Brotzen, Olga M., 2024: A new Lagerstätte-like fossil assemblage from the early Silurian of Mösseberg, Sweden. (45 hp)

676. Eng, Simon, 2024: Precursors to the South Atlantic Anomaly - Magnetic field variations in Lake Eilandvlei, South Africa. (45 hp)

677. Husén, Simon, 2024: Structural Geological Model of the Kaunisvaara Mining District, Norrbotten, Sweden. (45 hp)

678. Hjalmarsson, Tilda, 2024: Det underkambriska problematiska fossilet *Spatangopsis* - Vad är dess verkliga affinitet? (15 hp)

679. Kuberna, Marcos, 2024: En litteraturstudie om klorparaffiner i grundvattnet och dess implikationer på hälsa och miljö. (15 hp)

680. Persson, Viktor, 2024: Litteraturstudie: HIMU ursprung och framtid. (15 hp)

681. Selin, Sigrid, 2024: Hur kan paleoekologiska studier hjälpa oss att bättre förstå hur de ekosystem vi anser skyddsvärda har formats och hur de bör vårdas? (15 hp)

682. Rey, August, 2024: Isrörelser och havstransgressioner speglade i Kåsebergåsen. (15 hp)

683. von Vultée, Anton, 2024: Babets kvarlevor - En morfologisk och sedimentologisk undersökning av överspolningssediment vid Tobisvik, Simrishamn. (15 hp)

684. Olsson Roso, Céline, 2024: Fåglarnas ursprung och tidiga utveckling. (15 hp)

685. Nawrocki, Bartosz, 2024: Karaktärisering av Cr-spinell i den ordoviciska Lokaformationen vid Skultorps stenbrott, Billingen. (15 hp)

686. Rydh, Alexander, 2024: Unraveling Magnetic Anomalies: A Study of Earth's Field Asymmetries during the Laschamps Excursion. (15 hp)

Lunds universitet